*Revised manuscript with no changes marked
Click here to view linked References

Modelling biogeochemical processes and isotope fractionation of Enhanced *in situ* Biodenitrification in a fractured aquifer

Paula Rodríguez-Escales[1,2*], Albert Folch[3,4,5], Georgina Vidal-Gavilan[1,2], Boris M. van Breukelen[6]

1 d D'ENGINY biorem S.L., C. Madrazo 68, 08006 Barcelona, Spain.

2 Grup de Mineralogia Aplicada i Geoquímica de Fluids, *Departament de Cristal·lografia, Mineralogia i Dipòsits Minerals, Facultat de Geologia, Universitat de Barcelona (UB), C/Martí Franquès, S/N, Barcelona (Spain).*

3 Department of Civil and Environmental Engineering, Universitat Politècnica de Catalunya (UPC), c/Jordi Girona 1-3, 08034 Barcelona, Spain.

4 Unitat Associada: Grup d'Hidrologia Subterrània (UPC-CSIC)

5 Institut de Ciència i Tecnologia Ambientals (ICTA), Universitat Autònoma de Barcelona (UAB), Bellaterra, Barcelona 08193, Spain.

6 Department of Watermanagement, Faculty of Civil Engineering and Geosciences, Delft University of Technology

(*) Present address: Grup d'Hidrologia Subterrània (UPC-CSIC), Civil and Environmental Engineering Department. Universitat Politècnica de Catalunya-BarcelonaTech, Jordi Girona 1-3, Mòdul D-2, 08034 Barcelona, Spain.

Abstract

Enhanced *in situ* biodenitrification (EIB) is a feasible technology to clean nitrate-polluted groundwater and reach drinking water standards. Aimed at enabling a better monitoring and management of the technology at the field scale, we developed a two-dimensional reactive transport model (RTM) of a cross section (26.5 x 4 m) of a fractured aquifer composed of marls involving both biogeochemical processes and associated isotope fractionation. The RTM was based on the upscaling of a previously developed batch-scale model and on a flow model that was constructed and calibrated on *in situ* pumping and tracer tests. The RTM was validated using the experimental data provided by Vidal-Gavilan et al. (2013). The model considers several processes including (i) exogenous and endogenous microbial nitrate and sulfate respiration coupled to ethanol oxidation and linked to microbial growth and decay, and (ii) geochemical interactions (dissolution/precipitation of calcite), and (iii) isotopic fractionation of the reaction network ($^{15}N\text{-}NO_3$, $^{18}O\text{-}NO_3$, ^{13}C-DIC, ^{13}C-Ethanol, ^{13}C-Biomass, and ^{13}C-Calcite). Most of the calibrated microbiological parameter values at field scale did not change more than one order of magnitude from those obtained at batch scale, which indicates that parameters determined at the batch scale can be used as initial estimates to reproduce field observations provided that groundwater flow is well known. In contrast, the calcite precipitation rate constant increased significantly (fifty times) with respect to batch scale. The incorporation of isotope fractionation into the model allowed to confirm the overall consistency of the model and to test the practical usefulness of assessing the efficiency of EIB through the Rayleigh equation approach. The large underestimation of the Rayleigh equation of the extent of EIB (from 10 to 50 %) was caused by the high value of hydrodynamic dispersion observed in this fractured aquifer together with the high reaction rates.

Keywords

Denitrification; Groundwater; Calcite precipitation; Reactive transport modeling; Up-scaling

1 Introduction

Nitrate is one of the most prevalent and common groundwater contaminants (European Environment Agency, 2007; Organisation for Economic Co-operation and Development, 2008; Rivett et al., 2008). Excessive ingestion of nitrates from polluted drinking water and their subsequent conversion to nitrites can induce methemoglobinemia in humans and potentially play a role in the development of cancers (Fan and Steinberg, 1996; Fewtrell, 2004; Höring and Chapman, 2004). Therefore, the European Union has established maximum concentrations of nitrate and nitrite in drinking water of 50 mg/l for nitrate and 0.5 mg/l for nitrite. The proportions of groundwater bodies at high risk of nitrate pollution (showing mean nitrate concentrations greater than 25 mg/l) were reported as 80% in Spain, 50% in the UK, 36% in Germany, 34% in France and 32% in Italy (European Environment Agency, 2007). The high nitrate concentrations decrease the availability of water for domestic uses. Consequently, many water supply wells have been abandoned (Gierczak et al., 2007). Due to its minimal cost, the most common solution to nitrate pollution has been to mix polluted and clean groundwater. Nevertheless, this solution is extremely limited by water scarcity in Mediterranean and/or (semi-) arid countries, a situation that will become worse due to climate change (IPCC, 2007). Even in countries with no water shortage problems, there is often a lack of clean water to mix and dilute groundwater with high nitrate concentrations (Stuart et al., 2011; Veraart et al., 2014). In this context, it is necessary to implement other solutions to improve the quality of the groundwater.

Many technologies are available for treating nitrate in groundwater, such as reverse osmosis, ion exchange, electrodialysis, and chemical and biological denitrification (McAdam and Judd, 2007; Schnobrich et al., 2007; Ricardo et al., 2012). Most of these technologies focus on *ex situ* treatments, which are inherently more expensive than *in situ* treatments due to energy consumption and the interference with surface activities (e.g., building a treatment plant) (Della Rocca et al., 2007). Biological denitrification, which is known as Enhanced *In situ*

66 Biodenitrification (EIB), has environmental and economic advantages over other methods
67 because it is simple, selective, and cost effective (Smith et al., 2001). EIB is defined as a process
68 in which organic carbon is injected into the groundwater through injection wells to enhance
69 microbial denitrification. During this process, nitrate is reduced to dinitrogen gas by anaerobic
70 facultative bacteria that use nitrate as the electron acceptor and that are ubiquitous in surface
71 water, soil and groundwater (Beauchamp et al., 1989). This technology is feasible for cleaning
72 nitrate-polluted groundwater and meeting drinking water standards (Matějů et al., 1992; Khan
73 and Spalding, 2004; Vidal-Gavilan et al., 2013).

74 Geochemical interactions occur between the biodenitrification reactants and the porous
75 geological medium in response to biodegradation reactions. These interactions may play a
76 critical role in the implementation of EIB in aquifers. Because of the production of dissolved
77 inorganic carbon (DIC) and pH alteration, carbonate mineral dissolution/precipitation is
78 induced by changes in the initial hydrogeological and hydrochemical properties of the aquifer
79 by heterotrophic biodenitrification (Rodríguez-Escales et al., 2014). Moreover, dinitrogen gas
80 production can lead to a modification of the hydraulic conductivity (Amos and Mayer, 2006).
81 These changes can modify the hydrogeological characteristics of the aquifer and modify the
82 efficiency of the groundwater treatment (Noiriel et al., 2012).

83 Another important factor when monitoring EIB in the field is the dilution caused by
84 hydrodynamic dispersion of nitrate rich water and water with lower nitrate levels (e.g.,
85 recharge). Even without any entrance of clean groundwater, dilution will occur in the fringe of
86 the cleaned groundwater plume from EIB and polluted groundwater. Because of dilution, a
87 decrease in nitrate concentration cannot always be attributed to degradation. Monitoring the
88 changes in the nitrogen and oxygen isotope ratios of nitrate ($\delta^{15}N\text{-}NO_3^-$ and $\delta^{18}O\text{-}NO_3^-$) allows
89 the degradation to be identified (Otero et al., 2009; Puig et al., 2013; Carrey et al., 2014) and
90 therefore nitrate transformation and dilution to be distinguished. In EIB applications, this
91 distinction improves the characterization of the clean groundwater plume and allows nutrient

injection to be optimized, reducing treatment costs. As NO_3^- is consumed, the residual NO_3^- becomes enriched in the heavy isotopes ^{15}N and ^{18}O, and the denitrification reaction follows a Rayleigh distillation process (Eq.1):

$$R_S = R_{S,0}\, f^{(\alpha-1)} \quad (1)$$

where R_s is the stable isotope ratio (i.e., $^{15}N/^{14}N$; $^{18}O/^{16}O$) of the fraction of molecules remaining, f; $R_{s,0}$ is the initial isotopic composition of the molecule; and α is the kinetic isotopic fractionation factor of the transformation process, which is often represented as the kinetic isotopic enrichment factor ε (in permil, ‰), where ε = (α-1).

Despite that many studies have characterized the isotopic processes associated with biodenitrification by using the Rayleigh equation, some of the most recent works have shown that this equation does not always give accurate results at the field scale (Abe and Hunkeler, 2006; van Breukelen, 2007; van Breukelen and Prommer, 2008; Green et al., 2010; van Breukelen and Rolle, 2012). It must be mentioned that all of these studies focused on natural attenuation processes while none on enhanced biodenitrification and fractured aquifers. The differences between Rayleigh-determined and field-scale results are caused because the Rayleigh equation was developed for a closed system (van Breukelen, 2007) and does not account for hydrodynamic dispersion that tends to attenuate isotopic variations. These limitations have been addressed by incorporating isotope fractionation processes into numerical or analytical reactive transport models that account for hydrodynamic dispersion (van Breukelen and Prommer, 2008).

In addition to nitrate isotopes, other isotopes such as carbon isotopes are also involved in EIB, and can help to quantify the reaction network (biological reactions and geochemical interactions). The inclusion of dissolved inorganic carbon isotopes (δ^{13}C-DIC) into the biogeochemical model, which are involved in both direct (oxidation of organic carbon) and indirect processes (carbonate mineral interaction) of enhanced biodenitrification, is expected

117 to allow better evaluations of the consistency of the model due the central role that δ^{13}C-DIC
118 plays in the overall reaction network (Rodríguez-Escales et al., 2014).

119 In this context, a field-scale reactive transport model (RTM) of EIB integrating hydrology,
120 microbiology, geochemistry, and isotope fractionation can provide significant benefits for the
121 planning, characterization, monitoring and optimization of this technology in field applications.
122 The integration of all the processes allows the evaluation of their relationships with each other
123 and the prediction of secondary processes such as induced mineral precipitations or
124 dissolution.

125 Several studies have evaluated biodenitrification using numerical models at different
126 scales (Smith et al., 2001; Chen and MacQuarrie, 2004; Lee et al., 2006; André et al., 2011;
127 Mastrocicco et al., 2011; Boisson et al., 2013). However, few studies have focused on
128 modelling enhanced biodenitrification (André et al., 2011; Mastrocicco et al., 2011; Boisson et
129 al., 2013), and only one study has been performed at the field scale (Boisson et al., 2013).
130 Furthermore, few studies have examined the effects of geochemical interactions on
131 biodenitrification within the aquifer matrix (Chen and MacQuarrie 2004) and only a few have
132 explored the potential use of isotope fractionation for monitoring biodenitrification (Lehmann
133 et al., 2003; Chen and MacQuarrie, 2004).

134 The models that have evaluated biodenitrification at the field scale (Chen and
135 MacQuarrie, 2004; Lee et al., 2006; Boisson et al., 2013) do not consider all of the processes
136 involved. The most complete model, which was presented by Chen and MacQuarrie (2004),
137 was applied to a sedimentary aquifer under natural attenuation conditions and did not take
138 into account all of the isotopes modified by biodenitrification (only ^{15}N-NO_3). Furthermore, no
139 field integrated model described flow and transport through fractured media, which are
140 characterized by higher heterogeneity with more complex hydrological conditions. Only one
141 model has been developed for this type of geological formation, but it concerns the simulation
142 of push-pull test involving only microbiological processes (Boisson et al., 2013).

Because of this lack of knowledge, the aim of this paper is to develop a reactive transport model that considers microbiological processes, geochemical interactions, and complete isotope geochemistry during EIB in a fractured media at the field scale. In fractured aquifers, hydrogeological parameters such as heterogeneity, connectivity between the fracture networks, flow dynamics, and porosity differ notably from those in more extensively tested alluvial aquifers and may pose difficulty for the modeling of *in situ* technologies. The model focuses on microbiological processes, such as exogenous and endogenous nitrate and sulfate respiration coupled with microbial growth and decay, geochemical processes, such as the precipitation of calcite, nitrate isotopic fractionation, including $\delta^{15}N\text{-}NO_3^-$ and $\delta^{18}O\text{-}NO_3^-$, and carbon isotope interactions. In addition, once the model was constructed, the extent of biodenitrification using nitrate isotopes was also evaluated with the Rayleigh equation to assess its use from a practical perspective in EIB applications. To our knowledge, this is the first reactive field-scale model of EIB in the literature which considers microbiological, geochemical, and isotopic processes in one integrated model.

2 Materials and Methods

2.1 Field site description and model code

The model aimed to simulate a slug injection experiment conducted as part of an EIB field experiment described in Vidal-Gavilan et al. (2013). EIB was carried out in an unconfined, carbonated, and well-connected fractured aquifer using ethanol as the organic carbon source. The site was located in the central part of the Osona region (442270, 4647255 UTM31/ETR89; 100 km north of Barcelona, Spain). The aquifer, with an extent 1260 km^2, is recognized as being vulnerable to nitrate pollution due to the large amount of pig farming in the area and the shallow water table. Nitrate levels in the groundwater have reached 200 mg/L or more for the last 10-20 years (Otero et al., 2009), and the natural attenuation rates in the aquifer were not sufficient to guarantee safe water (Otero et al., 2009). The experimental site covers an

169 area of approximately 1000 m^2 and was monitored with six full screened piezometers with an
170 average depth of 12.5 m.b.s. (432.5 m a.s.l.) (Fig. 1). The screening levels covered the aquifer
171 thickness (4-5 m). Before application of EIB, pumping and bromide-tracer tests were carried
172 out to characterize the hydrogeological parameters and flow conditions. The pumping test
173 indicated good connectivity between the boreholes despite being in a fractured aquifer. It also
174 indicated a relatively homogeneous effective permeability of approximately 5 m/d. To
175 determine the flow velocity and dispersivity, a tracer test was performed with bromide
176 (conservative ion) under natural flow conditions. IP-1 was used as the injection point of the
177 bromide, and MW-2 and MW-3 were used as observation wells. Bromide was monitored at
178 three depths (11 m m.b.s., 12 m.b.s., 13 m.b.s.), which covers the full depth of the
179 piezometers. The results of these field tests indicated that this fractured media could be
180 assumed as an equivalent porous medium with a faster flow in the depth between IP-1 and
181 MW-2 (described in subsection 2.2). An extended description of the field site can be found in
182 section 1 of the supporting information.

183 The EIB was performed for five months and then stopped. Once the background
184 concentration of nitrate had recovered (120 mg NO_3^-/L, 1.9 mM), a slug injection of ethanol
185 was performed. The presented model was focused on this slug injection and its subsequent
186 monitoring during two days. During the slug injection a total volume of ethanol solution of 1
187 m^3 was injected. The concentration was 630 mg/l of ethanol and it was assumed that its
188 entrance to the aquifer was similar throughout the screened interval of the injection well. The
189 injected solution was prepared at the surface using groundwater from an upstream well with
190 the same hydrochemical composition. All denitrification experiments were developed under
191 natural flow conditions. An extended description of the experiment is detailed in the
192 supporting information.

193 The model code used was PHAST (Parkhurst et al., 2010). This code was used both for
194 conservative and reactive transport simulations. PHAST couples the flow simulator HST3D and
195 the geochemical model PHREEQC-2 (Parkhurst and Appelo, 1999).

196 ## 2.2 Conservative transport

197 The conservative transport model was constructed based on the bromide tracer test.
198 Because the field tests demonstrated that this fracture medium could be assumed to be an
199 equivalent porous medium, we used the transport equations for porous media. PHAST solved
200 the conservative transport model following equation 2:

201 $$\phi \frac{\partial c_i}{\partial t} = -q\nabla c_i + \phi\nabla(D\nabla c_i) \quad (2)$$

202 where D is the dispersion tensor [L^2T^{-1}], q is the Darcy's velocity ([LT^{-1}] which is related to
203 hydraulic conductivity [LT^{-1}] and groundwater gradient [-]), ϕ is the porosity [-]. The model was
204 solved under transient conditions. The geometry of the model involved a cross section (2D)
205 between the injection point (IP) and monitoring well 3 (MW-3) (located 26.5 m from the IP)
206 along the groundwater flow direction and considered a saturated thickness of 4 m (Fig. 1). The
207 aquifer was treated as unconfined with constant heads and concentrations on the up-gradient
208 and down-gradient boundaries (8.51, 8.57 m.b.s.). Constant head values were assigned to
209 simulate the hydraulic gradient observed during the field experiments (2.3 x 10^{-3}). Because
210 there was not any other flow except the slug injection (e.g. rainfall, external pumping), zero
211 flow conditions were assigned to the upper and bottom boundaries.

212 Simulations were carried out with a hydraulic conductivity of 7.5 m/d and an effective
213 porosity of 7x10^{-4}, both values are in the range of parameters obtained in the field. The faster
214 flow at depth between the injection point (IP) and MW-2 was characterized by a higher
215 hydraulic conductivity (32 m/d)). The average groundwater flow velocity was approximately 30
216 m/d. The model was calibrated using two dispersivity coefficients depending on the distance
217 to the injection point (1.4 m from 0 to 12.5 m in the domain and 6.5 m from 12.5 to 26.5 m (in

X axis)). Then following the Peclet and Courant numbers (Eq. 2 and 3, respectively), we used a uniform 0.5 x 0.1 m grid and a time step of 0.005 days (total time was 3.5 d).

$$C = \frac{\Delta l}{\alpha} < 2 \quad (3)$$

$$Pe = \frac{v\Delta t}{\Delta l} < 1 \quad (4)$$

where Δl is the size of the cell (length and height) [L], α is the dispersivity coefficient (longitudinal or vertical) [L], v is the groundwater velocity [LT^{-1}], and Δt is the time step [T].

2.3 Biogeochemical reactive transport model

When the conservative model was finished, reactive processes were added to the same PHAST model. Since PHAST uses the original PHREEQC-2 database syntax, arbitrary equilibrium and non-equilibrium reaction networks were defined as in Rodríguez-Escales et al. (2014) which simulated EIB at batch scale with PHREEQC. Kinetic reactions such as ethanol degradation, bacterial growth and decay, calcite precipitation, and all the isotopic reactions not being part of the standard database, were incorporated into the module in the form of simple BASIC routines, following the equations described in Table 1 (Equations 5-8). For equilibrium reactions, the reaction constants were used directly as provided by the PHREEQC-2 standard database. The model was run in transient conditions considering the initial heads measured before the biodenitrification started.

2.3.1 Microbiological processes

Both nitrate and sulfate respiration coupled to microbial growth were modeled using double Monod kinetics (Table 1). The stoichiometric relationships were based on Reactions 1 and 2, which summarize the redox respiration reaction in nitrate and sulfate reduction coupled with microbial growth. In those reactions, the biomass was considered to have an average chemical composition of $C_5H_7O_2N$ (Porges et al., 1956). The portions of the substrate's electrons used for cell synthesis during these anoxic processes were assumed to be 0.682 and

242 0.882 moles C-biomass/moles C-ethanol for denitrification and sulfate-reduction, respectively,
243 based on the calculations described in (McCarty, 1975).

244 $0.083\ C_2H_5OH + 0.088\ NO_3^- + 0.044\ H^+ = 0.024\ C_5H_7O_2N + 0.032\ N_2 + 0.045\ HCO_3^- + 0.164\ H_2O$

245 Reaction 1

246 $0.083\ C_2H_5OH + 0.022\ SO_4^{2-} + 0.018\ N_2 + 0.044\ H^+ + 0.012\ CO_2 = 0.022\ H_2S + 0.036\ C_5H_7O_2N + 0.125\ H_2O$

247 Reaction 2

248 The model incorporated two types of biomass: the denitrifier and the sulfate reducing
249 biomass. Both types of biomass were assumed to remain attached to the sediment. Because
250 the model was focused on a system with a mature biofilm, the initial value of the denitrifier
251 biomass used in the model was taken as the maximum value of the biomass simulated in a
252 previous batch model using the same composition groundwater of the field site (Supporting
253 Information). The initial value was 8×10^{-4} M, and we applied the same initial concentration for
254 both types of biomass. This approach was also followed by Tang et al. (2013), who used the
255 same initial value for different populations (denitrifiers, Fe reducers, sulfate reducers,
256 fermenters and methanogens) in a model of uranium redox transformation.

257 **2.3.2 Geochemical processes**

258 The main abiotic geochemical process considered was calcite precipitation since
259 Rodríguez-Escales et al. (2014) observed that when ethanol was used as the organic carbon
260 source, calcite precipitation was induced. The precipitation rate was modeled using
261 expressions 8-9 from Table 1. Potential changes in porosity due to calcite precipitation were
262 calculated using the Equation 10.

263 $$\Delta\phi(\%) = \left(\frac{V_o - \left(\frac{M_{cc}}{\rho_{cc}} \right)}{V_t} \right) x\ 100 \qquad (10)$$

264 where ϕ is the porosity [-], V_o is the initial void volume [L^3], ρ_{cc} is the calcite density [$M\ L^{-3}$], M_{cc}
265 is mass of precipitated calcite [M],and V_t is total volume [L^3].

Degassing of N_2, which is the most important gas in denitrification processes, was evaluated calculating its partial pressure and comparing it with total hydrostatic pressure which was 1 atm at the water table and 0.1 higher per 1 m depth below the water table (it was an unconfined aquifer). When the total pressure (the sum of partial pressures of the various gases) was higher than hydrostatic pressure, it was considered that degassing could occur in the aquifer.

2.3.3 Stable isotope geochemistry model

The isotopic fractionation of nitrogen and oxygen in nitrate and of carbon in C-containing compounds was included in the model. Assuming Monod degradation kinetics, the rates of the heavy ($^{15}N\text{-}NO_3^-$, $^{18}O\text{-}NO_3^-$, ^{13}C-ethanol) and light ($^{14}N\text{-}NO_3^-$, $^{16}O\text{-}NO_3^-$, ^{12}C-ethanol) isotopes from the batch experiment were modeled as described in (van Breukelen and Prommer, 2008) (Equations 10-11 from Table 1). The nitrate enrichment factor was based on Vidal-Gavilan et al. (2013) (-12.9 ‰ and -8.8 ‰ for the nitrogen and oxygen of nitrate, respectively). The carbon isotope fractionation of ethanol during denitrification was taken from Rodríguez-Escales et al. (2014) (ε =+8 ‰). Because these enrichment factors were determined under laboratory conditions (closed system), they were only affected by degradation processes, and they could be used at the field scale (Torrentó et al., 2011; Carrey et al., 2013). Furthermore, laboratory conditions were very similar to field conditions: the groundwater and sediments used were taken from the site and the *in-situ* groundwater temperature (15ºC) was maintained. Nevertheless, to our knowledge, the enrichment factor for ethanol during sulfate reduction has not yet been reported in the literature. The most similar conditions were found in Goevert and Conrad (2008). They determined the enrichment factors for the oxidation of acetate by heterotrophic sulfate-reducers (range between ε=+1.8 ‰ and -19.1 ‰). We used these values because acetate is a metabolite of ethanol in many sulfate reduction metabolisms (Nagpal et al., 2000). The large difference between the two fractionation factors from the different metabolic pathways that the sulfate reducers used to

292 reduce the acetate (Goevert and Conrad, 2008). Note that enrichment factors might be
293 dependent on temperature (Elsner, 2010). Therefore, we determined the enrichment factor
294 for ethanol oxidation during denitrification at the *in-situ* groundwater temperature of 15°C.
295 With respect to the ethanol oxidation coupled to sulfate-reduction, the enrichment factors
296 were only available at 30 and 37°C. Therefore, we applied the lower and higher end of the
297 range (ε=+1.8 ‰ and -19.1 ‰) and expect that any influence of temperature is captured by
298 this wide range.

299 The carbon isotope network was based on Rodríguez-Escales et al. (2014), who extended
300 the model of van Breukelen et al. (2004), which is summarized in Figure 2 and Table 2. Note
301 that in this model the isotopic effect in the organic carbon (ethanol) was simplified to one
302 value that was representative of overall metabolism. Compared to the batch models of
303 Rodríguez-Escales et al. (2014), we also included the oxidation of ethanol due to sulfate
304 reduction and the decay of sulfate-reducing biomass. To simplify the model and because CO_2
305 degassing was not quantitatively important (results not shown), we considered that the
306 contribution of degassing to ^{13}C-DIC was negligible and then it was not included in the
307 numerical model. The model was calibrated with the δ^{13}C-DIC observations.

308 The δ^{13}C contents of heterotrophic biomass (e.g. *Pseudomonas aeruginosa)* have been
309 found to vary from -10.3 to -25.4 ‰ (Blair et al., 1985; Coffin et al., 1990). We adopted -20 ‰
310 for both the denitrifiers and sulfate-reducers. For calcite precipitation, the δ^{13}C-DIC
311 modification was calculated following the procedure of van Breukelen et al. (2004). They
312 calculated the δ^{13}C-$CaCO_3$ precipitation by applying the equilibrium fractionation factors to the
313 different inorganic carbon species and calcite (as defined by Mook (2000)). At 15°C, $^{13}\varepsilon_{a/b}$ was -
314 10.12 ‰, $^{13}\varepsilon_{c/b}$ was -0.49, and $^{13}\varepsilon_{s/b}$ was +0.41, where *a* is the dissolved CO_2, *b* is the dissolved
315 HCO_3^-, *c* is the dissolved CO_3^{-2}, and *s*is the solid calcite. Considering these fractionation factors
316 and the initial δ^{13}C-DIC value, we calculated an initial δ^{13}C-$CaCO_3$ value of -11.3 ‰. This value
317 was in the range described by Mook (2000).

2.3.4 Evaluation of the extent of Enhanced *in situ* Biodenitrification: RTM *versus* Rayleigh equation

In order to evaluate the use of the Rayleigh equation to determine the extent of biodenitrification from a practical perspective in field-scale EIB applications, we compared results from the RTM with those from the Rayleigh equation. In general, the extent of biodegradation (B%) is related to the fraction of degradation of the target pollutant, in this case nitrate (Eq. 16).

$$B\ (\%) = (1 - f_{deg}) x100 \tag{16}$$

where f_{deg} is the remaining fraction of the target compound compared with initial concentration as a consequence of degradation.

For the case where the extent of biodegradation is calculated using the Rayleigh equation, $B_{Rayleigh}$ (%), the degradation fraction ($f_{deg,\ Rayleigh}$) was related to the simulated isotope signals (Eq. 17) (van Breukelen, 2007).

$$f_{deg,\ Rayleigh} = e^{\Delta/\varepsilon} \tag{17}$$

where Δ (%) represents the isotopic shift of a sample with respect to the source (= δ_S - $\delta_{S,0}$), and ε represents the kinetic isotopic enrichment factor, ε (‰). The extent of biodegradation calculated using the RTM, B_{RTM} (%), was calculated by comparing the nitrate concentration with the initial one in time (Eq. 18), and B_{RTM} (%) was calculated using equation 16.

$$f_{deg,\ RTM} = \frac{[NO_3^-]}{[NO_3^-]_0} \tag{18}$$

where $[NO_3^-]$ is nitrate concentration $[ML^{-3}]$ and $[NO_3^-]_0$ is the initial concentration of nitrate in aquifer (1.9×10^{-3} ML^{-3}).

The difference between the extents of EIB calculated by the Rayleigh equation and the RTM is evaluated by the theta value, Θ (Eq. 19). This approach was used in several studies to calculate the underestimation of the (assumed) first order rate constant, since –kt=ln(f), where f is the fractionation of contaminant remaining due to biodegradation (Abe and Hunkeler, 2006; van Breukelen and Prommer, 2008).

$$\theta = \left(1 - \frac{k_{Rayleigh}}{k_M}\right) \times 100 = \left(1 - \frac{\ln f_{deg,Rayleigh}}{\ln f_{deg,RTM}}\right) \times 100 \quad (19)$$

When Θ equals 0% the Rayleigh equation predicts an equal extent of EIB as calculated in the model. However, Θ usually > 0% and the Rayleigh equation underestimates the extent of degradation. For example, if Θ is 50% or 90%, the Rayleigh equation underestimates the actual extent of EIB (expressed at the pseudo first-order rate constant) with a factor 2 or 10, respectively. Theta values are discussed considering the Peclet number (Pe) (Eq. 4) and the Damkhöler number (Da) (Eq. 20),

$$Da = \frac{T_{adv}}{T_{reac}} \quad (20)$$

where T_{adv} is referred to advective time (distance divided by average velocity) and T_{reac} to characteristic time of reaction. This last one is defined similarly by Henze (2008) in Equation 21 and is valid when $K_{s,ED}$ is higher than the initial ED concentration.

$$T_{reac} = \frac{1}{k_{max}} \frac{K_{S,ED} + [ED]_0}{[X]_0} \frac{[EA]_0}{K_{S,EA} + [EA]_0} \quad (21)$$

where $[ED]_0$, $[EA]_0$, and $[X]_0$ are to initial conditions of the system, defined in Table 3.

2.4 Initial conditions and calibration process

The initial hydrochemistry and the temperature of the groundwater as well as of the injection groundwater are shown in Table 3. These concentrations were used as initial and boundary concentrations in the model. The sediment of the aquifer was composed of calcite (27.2 wt.%), muscovite ($KAl_2(AlSi_3O_{10})(OH)_2$, 26.2 wt.%), and quartz (23.1 wt.%), with small amounts of albite ($NaAlSi_3O_8$, 10.3 wt.%), dolomite (7.7 wt.%), sudoite ($Mg_2(Al; Fe^{3+})_3Si_3AlO_{10}(OH)_8$, 4.9 wt.%), and pyrite (0.6 wt.%) (Torrentó et al., 2011). In the model, we only considered calcite due to its intrinsic interaction with denitrification because of inorganic carbon production. Moreover, it was the major mineral in the sediment. All the calibrated model

parameters from both the conservative transport model (hydraulic conductivity, porosity, dispersivity) and the reactive transport model (maximum consumption rate, saturation constants, decay and precipitation rates) were manually calibrated. The initial values for the conservative model parameters were based on the values observed in the field tests and the model was calibrated taking into account the experimental bromide observations monitored at three different depths in piezometers MW-2 and MW-3 (Fig. 1). In the reactive model, the initial ones were based on a model of batch experiments using material from this site (Rodríguez-Escales et al. 2014). For the sulfate reduction process the initial parameters were taken from Nagpal et al. (2000), who modeled sulfate reduction by using ethanol as an organic carbon source in a batch system. The model was calibrated by fitting the measured concentrations (ethanol, nitrate, sulfate, calcium, dissolved inorganic carbon, pH, and isotope geochemistry ($\delta^{15}N\text{-}NO_3^-$; $\delta\ ^{18}O\text{-}NO_3^-$; $\delta^{13}C\text{-}DIC$)) and the saturation index of calcite in MW-2 and MW-3.

3 Results and discussion

3.1 Conservative transport model

The results of the conservative transport model are shown in Figure 3. Multilevel sampling indicated an earlier arrival of bromide in the deeper part of MW-2 (Fig. 3), whereas most of the bromide mass was detected at 0.14 d, a peak was observed at 0.05 d. Moreover, the concentration in the deeper part (reaching 20 mM) was twice those at shallower depths (approximately 10 mM). These differences in bromide concentration at different depths were not observed in MW-3, which indicates a homogenization of bromide transport along the flow line. Porosity was only related to the secondary porosity because groundwater flow occurs mainly through fractures (Vidal-Gavilan et al., 2013). The obtained dispersivity values (1.4 m (from 0 to 14 m of the domain) and 6.5 m (from 14 to 26 m)) were consistent with the scale

391 (26 m) of the biodenitrification application (Gelhar et al., 1992). Note the small increase of
392 bromide in MW-3 after day two (Fig. 3). We ascribe this increase to a slower groundwater flow
393 component as part of the fracture network with lower hydraulic conductivity or due to the
394 effects of the injection. Nevertheless, because the biodenitrification model extended for only
395 two days, this flow component was considered not quantitatively important and was not
396 included in the model.

397 3.2 Biogeochemical Reactive Transport Model

398 3.2.1 Microbiological processes

399 The RTM was performed taking the hydrogeological parameters determined in the
400 conservative transport model with refreshed head constants (8.54 and 8.42 m). In this case,
401 the head levels differed from the tracer test and the hydraulic gradient was higher;
402 consequently, the flow velocity increased. The flow velocity during the slug injection in most of
403 the domain was approximately 50 m/d.

404 Figure 4A shows the results of the 2D RTM for the upper and lower ends of wells MW-2
405 and MW-3 using the parameters from Table 4, all of them in the range of published data (Table
406 5). In general, the model fits well the general trend observed in the field and the modeled
407 values matched the observations. Both MW-2 and MW-3 showed decreasing nitrate
408 concentrations until non-detectable levels were present in less than 0.2 days. This rapid
409 reduction in concentration can be attributed to the high activity of biomass that had been
410 stimulated by ethanol during the previous five months. Both the exhaustion of ethanol and the
411 fast groundwater flow increased nitrate concentrations until they reached background levels in
412 MW-2. The modeled nitrate concentration at MW-3 began to increase after less than one day,
413 while the observed concentrations stayed at zero. The later breakthrough of nitrate observed
414 in the field was attributed to the slower flow component described for the tracer test results
415 that was not taken into account in the model (Fig. 3).

Undesired sulfate reduction was observed during the slug test, albeit the concentration of injected ethanol was chosen such that only nitrate should deplete. The observed sulfate decreased over time with 0.36 mM in MW-3 (Fig. 4c and 4c'), and H_2S was detected in MW-2 and MW-3 odor detection. Note that the ethanol peak matched in time with the decrease of sulfate (Fig. 4). Thus, this anaerobic activity was mainly attributed to an applied excess of ethanol in the subsurface.

During the upscaling process (in calibration process), the parameters were adjusted by considering the difference between the bioavailability of nutrients at the batch and field scales (based on the half-saturation constants) and the adaptation of microbial metabolism to the environment (based on decay constants) (Jin et al., 2012). Table 4 shows that the differences in the half-saturation parameters between the batch and field experiments are always less than one order of magnitude, except for the half-saturation of nitrate during denitrification. The decay constant in the field was higher than that from the laboratory (Table 4) because the biomass used in the batch experiments was younger (seven days) than that used at the field scale (five months). Considering the high variability of these parameters (Table 5), we believe that the differences observed between the parameters at the batch and field scales are small enough to set up the batch scale parameters as a good initial approximation to start up in the field scale models.

In contrast, the specific growth yields (Y_h) and the maximum rate constant (k_{max}) can be directly transferred from the laboratory to the field scale (Jin et al., 2012). Both parameters are related to the properties of enzymes and pathways of metabolic reactions that are the same in the laboratory and in the field (Table 4). Thus, these values can be directly extrapolated from the laboratory scale to the field scale.

3.2.2 Geochemical processes

Calcite precipitation was confirmed by the decrease of calcium in solution and the increase of the saturation index of calcite (Fig. 4g and 4g'). At this point, an increase in the

442 inorganic carbon in both MW-2 (from 9.5 to 10.8 mM) and MW-3 (from 9.5 to 11.4 mM) was
443 observed due to ethanol oxidation. The saturation index of calcite began at negative values but
444 became positive when inorganic carbon was added to the system due to ethanol oxidation.
445 The precipitation rate constant differed between batch scale (1×10^{-10} M/s) and field scale ($5 \times$
446 10^{-9} M/s) (Table 4). The value in the field was unexpectedly fifty times higher than that from
447 the laboratory experiments. This difference may have been caused by the sediment being
448 deposited in the reactor in the batch experiment, which limited the growth of calcite from the
449 standing solution to the crystals in the sediment. In the field the contact between groundwater
450 and the solid matrix was higher due to the transport of groundwater through the
451 microfractures. The field precipitation rate constant is consistent with the large range of values
452 from the literature (1.0×10^{-7}, 1.2×10^{-7}, and 2.3×10^{-10} M/s from Inskeep and Bloom (1985),
453 Busenberg and Plummer (1982) and van Breukelen et al. (2004), respectively).
454 The modeled values of pH slightly increased from 6.8 before injection to 7.1 (MW2) and 7
455 (MW3) following the injection (Fig. 4). The timing of this increase matched that of the increase
456 of the calcite saturation index in both piezometers. After 0.5-1 days, it recovered to the
457 previous value of 6.8. The overlapping in the error of the measured pH values does not allow
458 evaluating the basification of the media as shown by the modeled values (Fig. 4). The observed
459 field values may indicate that the system was buffered by the presence of carbonate minerals
460 which masked the effect of produced inorganic carbon from the EIB.
461 Regarding the degassing of dinitrogen gas, the results indicated that the sum of the
462 partial pressures were higher than hydrostatic pressure when denitrification occurred
463 indicating than degassing of the system could be induced (Fig. 5). Also, the degree of
464 overpressure due to denitrification was less than 1 bar. Considering the short time frame of
465 overpressure conditions in the studied aquifer section (≈ 1 day) we assumed for model
466 simplicity that the degree of actual degassing was limited and most of the produced N_2 gas
467 remained in dissolved state while flowing out of the aquifer section. The potential formation of

bubbles and how they change the hydraulic conductivity of the aquifer was thus not evaluated. Although we believe that formed gas was not trapped in this media because of the well connection between the horizontal and vertical fractures network, further research is needed.

Biofilm growth, microbial-induced mineral precipitation or dissolution and bubble formation can modify the hydrologic properties of the media (e.g., hydraulic conductivity, dispersivity and porosity) (Soares et al., 1991; Thullner, 2010). In our model, we assumed that the hydrologic properties of the media were constant due to the short duration of the field test (two days). In our case, the amount of biomass did not change significantly and remained at the same order of magnitude (Fig. 4) assuming bioclogging was negligible. The maximum relative change of porosity due to calcite precipitation at the end of the model (2 days) was less than 0.002% across the entire model domain. This change was calculated using Eq. 9. Then, calcite precipitation did not significantly modify the hydraulic properties either.

3.3 Stable isotope geochemistry model

The modeled N and O isotope ratios matched the observation data reasonably well in MW-2 (Fig. 6). The simulated delta values are only shown for nitrate concentrations that exceed 1 mg/ because analytical methods used in Vidal-Gavilan et al. (2013) for nitrate isotopes need a minimal concentration of nitrate similar to that concentration. In MW-2, the $\delta^{15}N\text{-}NO_3^-$ and $\delta^{18}O\text{-}NO_3^-$ values increased from 13.5 ‰ to 24.4 ‰ and from 5.8 to 12 between days 0.1 and 0.3 at the same time as nitrate decreased (Fig. 4a and 4a'). On the other hand, when the nitrate concentrations increased to the background values of the aquifer, the isotopic values also decreased to their initial values.

Variations of $\delta^{13}C$-DIC are controlled by the sources of carbon that are oxidized, including physical (e.g., CO_2 degassing, carbonate precipitation or dissolution) and biochemical processes (e.g., microbial respiration). Thus, all of the processes that affect the $\delta^{13}C$-DIC signal were included in the model, including the two types of respiration (exogenous and endogenous) for both nitrate and sulfate reduction and calcite precipitation. Although the

494 modeled values of δ^{13}C-DIC do not follow the general trend of the experimental field values,
495 they indicate the main processes that affect their variation (Fig. 7). Despite the important
496 fractionation due to the oxidation of ethanol and independent of the fractionation factor of
497 ethanol used in sulfate reduction, the δ^{13}C-DIC values did not change considerably (maximum
498 variation of 2 ‰) (Fig. 7, which only shows results of $\varepsilon_{eth/sulf}$=+1.8 ‰ because no difference
499 were between those and results using $\varepsilon_{eth/sulf}$=-19.1 ‰). The differences between the field and
500 modeled δ^{13}C-DIC changes were attributed to the natural variations of this isotope in
501 groundwater (the δ^{13}C-DIC values in the municipal well, which represent the natural
502 background, oscillated from -11 ‰ to -8 ‰ during the slug injection test). So, despite EIB
503 produces a change in the δ^{13}C values, natural variation in this site is much more important and,
504 consequently, the δ^{13}C variation becomes masked.

505 ## 3.4 Evaluation of the extent of Enhanced *in situ* Biodenitrification: RTM
506 ## *versus* Rayleigh equation

507 In this case study, the Rayleigh equation underestimates the extent of enhanced *in situ*
508 biodenitrification compared with the RTM simulations as it is observed in previous studies of
509 natural attenuation (Abe and Hunkeler, 2006; van Breukelen and Prommer, 2008; Green et al.,
510 2010; Lutz et al., 2013) (Fig. 8). The underestimation of the Rayleigh equation is associated
511 with its intrinsic limitation when used at the field scale (van Breukelen et al. 2007), where
512 other processes such as mixing, sorption or dispersion occur, compared to laboratory
513 experiments. In our case, we attributed the underestimation (from ten times to twice) to the
514 fractionation that occurs at the boundary between the groundwater cleaned by EIB and
515 polluted groundwater where mixing and dispersion processes are more important than in the
516 center of the plume (Fig. 8). Nevertheless, the spatial and temporal variations in the extent of
517 biodenitrification were qualitatively similar among RTM and Rayleigh equation results. This

518 indicates that from a practical point of view, the Rayleigh equation can be applied to obtain an
519 initial conservative estimate of the extent of EIB.

520 Figure 8 also shows that the extent of biodenitrification in different parts of the
521 denitrified groundwater plume and in time is underestimated by the Rayleigh equation to
522 different degrees (from 10-50 %). The T_{reac} and the T_{adv} are respectively 0.15 and 0.53 d, which
523 conform to a Da number of 3.6. The determined T_{reac} is very consistent with Figure 4, where
524 complete degradation was achieved in 0.2 d. On the other hand, the Peclet number was 200,
525 indicating that at this site the flow was highly advective. Considering these two values and Abe
526 and Hunkeler's (2006) work, the underestimation should be around 10%, which agrees with
527 the first stages of our case (until 0.8 d) where underestimation was between 10 and 30% (Fig.
528 8). Until this time the active plume of denitrification (with complete denitrification, see
529 percentage of degradation in Figure 8) still resided in the model domain. Nevertheless, when
530 the bulk of the denitrified plume moved outside of the model domain, underestimation
531 increased until 50%. This rise was associated with the relative importance of dispersion and
532 mixing processes in the upstream fringes of the plume. The degree of underestimation was
533 greater than those in other studies (Abe and Hunkeler, 2006; van Breukelen and Prommer,
534 2008; Lutz et al., 2013), most likely because of the considerably higher dispersivity coefficients
535 observed at our study site (around one order of magnitude higher than those studies
536 considering the scale of transport). Nonetheless, our results were in coherence with Green et
537 al. (2010) who determined that the apparent denitrification rate constant was 10 times lower
538 than the actual rate constant in case of highly heterogeneous aquifer conditions that induce
539 strong mixing processes.

540 In summary, the use of the Rayleigh equation in EIB applications will give a conservative
541 estimate of the degree of denitrification, but it will provide a stronger underestimate when
542 mixing processes are more important than reactions (e.g., in highly heterogeneous aquifers).

4 Conclusions

We developed a 2-D reactive transport model of EIB applied in a fractured aquifer that integrates biogeochemical processes as well as isotope fractionation to enable better planning, characterization, monitoring, and optimization of EIB. The reactive transport model was based on the upscaling of previous batch models that used groundwater and core material from the same experimental site. The microbiological processes were up-scaled based on adjustments of the half-saturation and decay constants. Most of the modified microbiological parameters did not differ by more than one order of magnitude, indicating that the initial batch values were a good approximation for the initial field scale modeling. In contrast, the calcite precipitation constant was 50 times larger than in the batch experiments. We attribute this difference to the different conditions between the laboratory and the field; whereas in laboratory, the sediment was deposited in the stagnant reactor hence limiting the growth of calcite, in field there was enhanced contact between groundwater and the solid matrix through the microfractures.

Although we assumed the hydraulic properties of the media to be constant over time, we quantified a relative decrease in porosity of less than 0.002% due to calcite precipitation. As the model was focused on the stationary phase of biofilm growth, porosity modification did not change considerably, and degassing was considered negligible. It is important to note that this decrease in porosity due to calcite precipitation was produced exclusively as a result of a slug injection of an organic carbon source. More research is needed to evaluate the relevance of bubble formation due to dinitrogen gas formation and how it can modify the hydraulic properties.

The integration of the isotope fractionation into the model allowed us to evaluate the overall model consistency. Compared to the batch scale, where denitrification produced significant changes on δ^{13}C-DIC, in this field work, δ^{13}C-DIC was mainly affected by the natural background variations, and changes due to enhanced bioremediation were not observed.

The degree of underestimation of the Rayleigh equation was low (less than 20%) and in agreement with Abe and Hunkeler (2006) when denitrification was going on. On the other hand, when most of the plume passed and denitrification rates became lower, the high dispersivity pushed the degree of underestimation to 50% in the upstream plume fringe. Despite this underestimation, the extents of biodenitrification were qualitatively similar in both the RTM and Rayleigh approaches. This indicates that from a practical point of view and considering its conservative behavior, the Rayleigh equation can be applied to EIB as an easy initial step to evaluate the extent of EIB.

Overall, the development of this integrated model allowed improving the knowledge of all the processes occurring during EIB at the field scale in a complex hydrogeological media. Although more research is needed to evaluate the behavior of EIB during long-term experiments, our model can be implemented in other field studies in order to evaluate the concentrations trends, to quantify the importance of secondary processes such calcite precipitation, or to evaluate if Rayleigh equation can be used to quantify the extent of denitrification in field applications.

5 Acknowledgments

We thank the anonymous reviewers for their comments and suggestions, which helped improve the quality of the manuscript. This work was financed by the CICYT projects CGL2014-57215-C4-1-R and CGL2014-57215-C4-2-R from the Spanish Government, MARSOL FP7-ENV-2013-WATER-INNO-DEMO from European Union and projects 2009SGR1030, 2009SGR1199 and TEM-2009 from the Catalan Government.

6 References

Abe, Y., Hunkeler, D., 2006. Does the Rayleigh equation apply to evaluate field isotope data in contaminant. Environ. Sci. Technol. 40, 1588-1596.

593 Amos, R.T., Mayer, K.U., 2006. Investigating the role of gas bubble formation and entrapment
594 in contaminated aquifers: Reactive transport modelling. J. Contam. Hydrol. 87, 123-154.
595 André, L., Pauwels, H., Dictor, M.C., Parmentier, M., Azaroual, M., 2011. Experiments and
596 numerical modelling of microbially-catalysed denitrification reactions. Chem. Geol. 287,
597 171-181.
598 Beauchamp, E.G., Trevors, J.T., Paul, J.W., 1989. Carbon Sources for Bacterial Denitrification.
599 in: Stewart, B.A. (Ed.). Adv. Soil S. Springer New York, pp. 113-142.
600 Blair, N., Leu, A., Munoz, E., Olsen, J., Kwong, E., Des Marais, D., 1985. Carbon isotopic
601 fractionation in heterotrophic microbial metabolism. Appl. Environ. Microbiol. 50, 996-
602 1001.
603 Boisson, A., de Anna, P., Bour, O., Le Borgne, T., Labasque, T., Aquilina, L., 2013. Reaction chain
604 modeling of denitrification reactions during a push–pull test. J. Contam. Hydrol. 148, 1-
605 11.
606 Busenberg, E., Plummer, L.N., 1982. The kinetics of dissolution of dolomite in CO_2-H_2O systems
607 at 1.5 to 65^{o}C and 0 to 1 atm PCO_2. Am. J. Sci. 282, 34.
608 Carrey, R., Otero, N., Soler, A., Gómez-Alday, J.J., Ayora, C., 2013. The role of Lower Cretaceous
609 sediments in groundwater nitrate attenuation in central Spain: Column experiments.
610 Appl. Geochem. 32, 142-152.
611 Carrey, R., Rodríguez-Escales, P., Otero, N., Ayora, C., Soler, A., Gómez-Alday, J.J., 2014. Nitrate
612 attenuation potential of hypersaline lake sediments in central Spain: Flow-through and
613 batch experiments. J. Contam. Hydrol. 164, 323-337.
614 Chen, D.J.Z., MacQuarrie, K.T.B., 2004. Numerical simulation of organic carbon, nitrate, and
615 nitrogen isotope behavior during denitrification in a riparian zone. J. Hydrol. 293, 235-
616 254.

617 Coffin, R.B., Velinsky, D.J., Devereux, R., Price, W.A., Cifuentes, L.A., 1990. Stable carbon
618 isotope analysis of nucleic acids to trace sources of dissolved substrates used by
619 estuarine bacteria. Appl. Environ. Microbiol. 56, 2012-2020.
620 Della Rocca, C., Belgiorno, V., Meriç, S., 2007. Overview of in-situ applicable nitrate removal
621 processes. Desalination 204, 46-62.
622 Elsner, M., 2010. Stable isotope fractionation to investigate natural transformation
623 mechanisms of organic contaminants: principles, prospects and limitations. J. Environ.
624 Monitor. 12, 2005-2031.
625 European Environment Agency, E., 2007. Present concentration of nitrate in groundwater
626 bodies in European countries, 2003.
627 Fan, A.M., Steinberg, V.E., 1996. Health implications of nitrate and nitrite in drinking water: an
628 update on. Regul. Toxicol. Pharmacol. 23, 35-43.
629 Fewtrell, L., 2004. Drinking-water nitrate, methemoglobinemia, and global burden of disease: a
630 discussion. Environ. Health Perspect. 112, 1371-1374.
631 Gelhar, L.W., Welty, C., Rehfeldt, K.R., 1992. A critical review of data on field-scale dispersion
632 in aquifers. Water Resour. Res. 28.
633 Gierczak, R., Devlin, J.F., Rudolph, D.L., 2007. Field test of a cross-injection scheme for
634 stimulating in situ denitrification near a municipal water supply well. J. Contam. Hydrol.
635 89, 48-70.
636 Goevert, D., Conrad, R., 2008. Carbon Isotope Fractionation by Sulfate-Reducing Bacteria Using
637 Different Pathways for the Oxidation of Acetate. Environ. Sci. Technol. 42, 7813-7817.
638 Green, C.T., Böhlke, J.K., Bekins, B.A., Phillips, S.P., 2010. Mixing effects on apparent reaction
639 rates and isotope fractionation during denitrification in a heterogeneous aquifer. Water
640 Resour. Res. 46.
641 Henze, M., 2008. Biological wastewater treatment: principles, modelling and design, London.

642 Höring, H., Chapman, D., 2004. Nitrates and nitrites in drinking water. In: World Health
643 Organization Drinkig Water Series.
644 Inskeep, W.P., Bloom, P.R., 1985. An evaluation of rate equations for calcite precipitation
645 kinetics at pCO2 less than 0.01 atm and pH greater than 8. Geochim. Cosmochim. Acta
646 49, 2165-2180.
647 IPCC, 2007. Climate change 2007: synthesis report.
648 Jin, Q., Roden, E.E., Giska, J.R., 2012. Geomicrobial Kinetics: Extrapolating Laboratory Studies
649 to Natural Environments. Geomicrobiol. J. 30, 173-185.
650 Khan, I.A., Spalding, R.F., 2004. Enhanced in situ denitrification for a municipal well. Water Res.
651 38, 3382-3388.
652 Lee, M.-S., Lee, K.-K., Hyun, Y., Clement, T.P., Hamilton, D., 2006. Nitrogen transformation and
653 transport modeling in groundwater aquifers. Ecol. Modell. 192, 143-159.
654 Lehmann, M.F., Reichert, P., Bernasconi, S.M., Barbieri, A., McKenzie, J.A., 2003. Modelling
655 nitrogen and oxygen isotope fractionation during denitrification in a lacustrine redox-
656 transition zone. Geochim. Cosmochim. Acta 67, 2529-2542.
657 Lutz, S.R., van Meerveld, H.J., Waterloo, M.J., Broers, H.P., van Breukelen, B.M., 2013. A
658 model-based assessment of the potential use of compound-specific stable isotope
659 analysis in river monitoring of diffuse pesticide pollution. Hydrol. Earth Syst. Sci. 17,
660 4505-4524.
661 Mastrocicco, M., Colombani, N., Salemi, E., Castaldell, G., 2011. Reactive modelling of
662 denitrification in soils with natural and depleted organic matter. Water, Air, Soil Pollut.
663 222, 10.
664 Matějů, V., Čižinská, S., Krejčí, J., Janoch, T., 1992. Biological water denitrification—A review.
665 Enzyme Microb. Technol. 14, 170-183.
666 McAdam, E.J., Judd, S.J., 2007. Denitrification from drinking water using a membrane
667 bioreactor: Chemical and biochemical feasibility. Water Res. 41, 4242-4250.

668 McCarty, P.L., 1975. Stoichiometry of biological rates. Prog. Water. Technol. 7, 157-172.
669 Mook, W.G., 2000. Environmental isotopes in the hydrological cycle. Principles and
670 applications. Volume I. Introduction: Theory, Methods, Review. UNESCO/IAEA, Vienna, p.
671 280.
672 Nagpal, S., Chuichulcherm, S., Livingston, A., Peeva, L., 2000. Ethanol utilization by sulfate-
673 reducing bacteria: An experimental and modeling study. Biotechnol. Bioeng. 70, 533-
674 543.
675 Noiriel, C., Steefel, C.I., Yang, L., Ajo-Franklin, J., 2012. Upscaling calcium carbonate
676 precipitation rates from pore to continuum scale. Chem. Geol. 318–319, 60-74.
677 Organisation for Economic Co-operation and Development, O., 2008. Environmental
678 performance of agriculture in OECD countries since 1990., p. 576.
679 Otero, N., Torrentó, C., Soler, A., Menció, A., Mas-Pla, J., 2009. Monitoring groundwater nitrate
680 attenuation in a regional system coupling hydrogeology with multi-isotopic methods:
681 The case of Plana de Vic (Osona, Spain). Agr. Ecosyst. Environ. 133, 103-113.
682 Parkhurst, D.L., Appelo, C.A.J., 1999. User's guide to PHREEQC (version 2) - a computer
683 program for speciation, reaction-path, 1D-transport, and inverse geochemical
684 calculations. in: 99-4259, W.-R.I.R. (Ed.). U.S. GEOLOGICAL SURVEY.
685 Parkhurst, D.L., Kipp, K.L., Charlton, S.R., 2010. PHAST Version 2—A program for simulating
686 groundwater flow, solute transport, and multicomponent geochemical reactions. in: 6–
687 A35, U.S.G.S.T.a.M. (Ed.), p. 235.
688 Porges, N., Jasewicz, L., Hoover, S., 1956. Principles of biological oxidation. In biological
689 treatment of sewage and industrial wastes. Reinhold. Publ., New York.
690 Puig, R., Folch, A., Menció, A., Soler, A., Mas-Pla, J., 2013. Multi-isotopic study (^{15}N, ^{34}S, ^{18}O,
691 ^{13}C) to identify processes affecting nitrate and sulfate in response to local and regional
692 groundwater mixing in a large-scale flow system. Appl. Geochem. 32, 129-141.

693 Ricardo, A.R., Carvalho, G., Velizarov, S., Crespo, J.G., Reis, M.A.M., 2012. Kinetics of nitrate
694 and perchlorate removal and biofilm stratification in an ion exchange membrane
695 bioreactor. Water Res. 46, 4556-4568.
696 Rivett, M.O., Buss, S.R., Morgan, P., Smith, J.W.N., Bemment, C.D., 2008. Nitrate attenuation in
697 groundwater: A review of biogeochemical controlling processes. Water Res. 42, 4215-
698 4232.
699 Rodríguez-Escales, P., van Breukelen, B., Vidal-Gavilan, G., Soler, A., Folch, A., 2014. Integrated
700 modeling of biogeochemical reactions and associated isotope fractionations at batch
701 scale: A tool to monitor enhanced biodenitrification applications. Chem. Geol. 365, 20-
702 29.
703 Schnobrich, M.R., Chaplin, B.P., Semmens, M.J., Novak, P.J., 2007. Stimulating
704 hydrogenotrophic denitrification in simulated groundwater containing high dissolved
705 oxygen and nitrate concentrations. Water Res. 41, 1869-1876.
706 Smith, R.L., Miller, D.N., Brooks, M.H., Widdowson, M.A., Killingstad, M.W., 2001. In situ
707 stimulation of groundwater denitrification with formate to remediate. Environ. Sci.
708 Technol. 35, 196-203.
709 Soares, M., Braester, C., Belkin, S., Abeliovich, A., 1991. Denitrification in laboratory sand
710 columns: Carbon regime, gas accumulation and hydraulic properties. Water Res. 25, 325-
711 332.
712 Stuart, M.E., Gooddy, D.C., Bloomfield, J.P., Williams, A.T., 2011. A review of the impact of
713 climate change on future nitrate concentrations in groundwater of the UK. Sci. Total
714 Environ. 409, 2859-2873.
715 Tang, G., Watson, D.B., Wu, W.-M., Schadt, C.W., Parker, J.C., Brooks, S.C., 2013. U(VI)
716 Bioreduction with Emulsified Vegetable Oil as the Electron Donor – Model Application to
717 a Field Test. Environ. Sci. Technol. 47, 3218-3225.

718 Thullner, M., 2010. Comparison of bioclogging effects in saturated porous media within one-
719 and two-dimensional flow systems. Ecol. Eng. 36, 176-196.
720 Torrentó, C., Urmeneta, J., Otero, N., Soler, A., Viñas, M., Cama, J., 2011. Enhanced
721 denitrification in groundwater and sediments from a nitrate-contaminated aquifer after
722 addition of pyrite. Chem. Geology. 287, 90-101.
723 van Breukelen, B.M., 2007. Quantifying the degradation and dilution contribution to natural
724 attenuation of contaminants by means of an open system rayleigh equation. Environ.
725 Sci. Technol. 41, 4980-4985.
726 van Breukelen, B.M., Griffioen, J., Röling, W.F.M., van Verseveld, H.W., 2004. Reactive
727 transport modelling of biogeochemical processes and carbon isotope geochemistry
728 inside a landfill leachate plume. J. Contam. Hydrol. 70, 249-269.
729 van Breukelen, B.M., Prommer, H., 2008. Beyond the Rayleigh Equation: Reactive Transport
730 Modeling of Isotope Fractionation Effects to Improve Quantification of Biodegradation.
731 Environ. Sci. Technol. 42, 2457-2463.
732 van Breukelen, B.M., Rolle, M., 2012. Transverse Hydrodynamic Dispersion Effects on Isotope
733 Signals in Groundwater Chlorinated Solvents' Plumes. Environ. Sci. Technol. 46, 7700-
734 7708.
735 Veraart, A.J., Audet, J., Dimitrov, M.R., Hoffmann, C.C., Gillissen, F., de Klein, J.J.M., 2014.
736 Denitrification in restored and unrestored Danish streams. Ecol. Eng. 66, 129-140.
737 Vidal-Gavilan, G., Folch, A., Otero, N., Solanas, A.M., Soler, A., 2013. Isotope characterization of
738 an in situ biodenitrification pilot-test in a fractured aquifer. Appl. Geochem. 32, 153-163.

739

Figure captions

Figure 1. Pilot test layout and cross section considered in the model (modified from Vidal-Gavilan (2013)). IP means Injection Point, and MW means Monitoring Well. The black lines in the cross section near MW-2 and MW-3 indicate the sampling depth.

Figure 2. Carbon isotope reaction network with different isotope fractionations and initial conditions.

Figure 3. Modeling of the bromide tracer test. Observations (data points: Δ, 434 m a.s.l.; ●, 435 m a.s.l.; □, 436 m a.s.l.) versus modeling results (lines) (dotted line, 434m.a.s.l.; --435 m a.s.l.; — 436m.a.s.l.).

Figure 4. Modeling results (lines) versus observations (●) for MW-2 and MW-3. Solid lines correspond to 434 m a.s.l., dashed lines correspond to 435 m a.s.l. Red lines correspond to sulfate-reducer biomass, and green lines represent the results of the conservative model without reactions.

Figure 5. Modeling results of partial pressure of dinitrogen gas (atm), dotted lines represent the hydrostatic pressure. When the sum of partial pressures, which are mainly governed by dinitrogen gas pressure (results not shown), are higher than hydrostatic pressure degassing exists.

Figure 6. Simulation of nitrate isotope data. Modeling results (lines) versus observations in MW-2. The results of nitrate isotopes are only shown for nitrate concentrations up to 0.2 mM, where nitrate isotopes analytics were trustworthy. Solid lines correspond to 434 m a.s.l., dashed lines correspond to 435 m a.s.l. and green lines represent the results of the conservative model without reactions.

Figure 7. Modelling results (lines) versus observations of δ^{13}C-DIC at MW-2 (A) and MW-3 (B). Solid lines correspond to 434 m a.s.l., dashed lines correspond to 435 m a.s.l. The plots correspond to different fractionation factors of ethanol due to sulfate reduction; A corresponds to MW-2 and B to MW-3.

766 **Figure 8.** Temporal-spatial variations of the extents of EIB (%) calculated using the Rayleigh
767 equation and the RTM, the underestimation of the extent of EIB following the Rayleigh
768 equation (theta (%)), and nitrate rate (mM/d).

Figure
Click here to download high resolution image

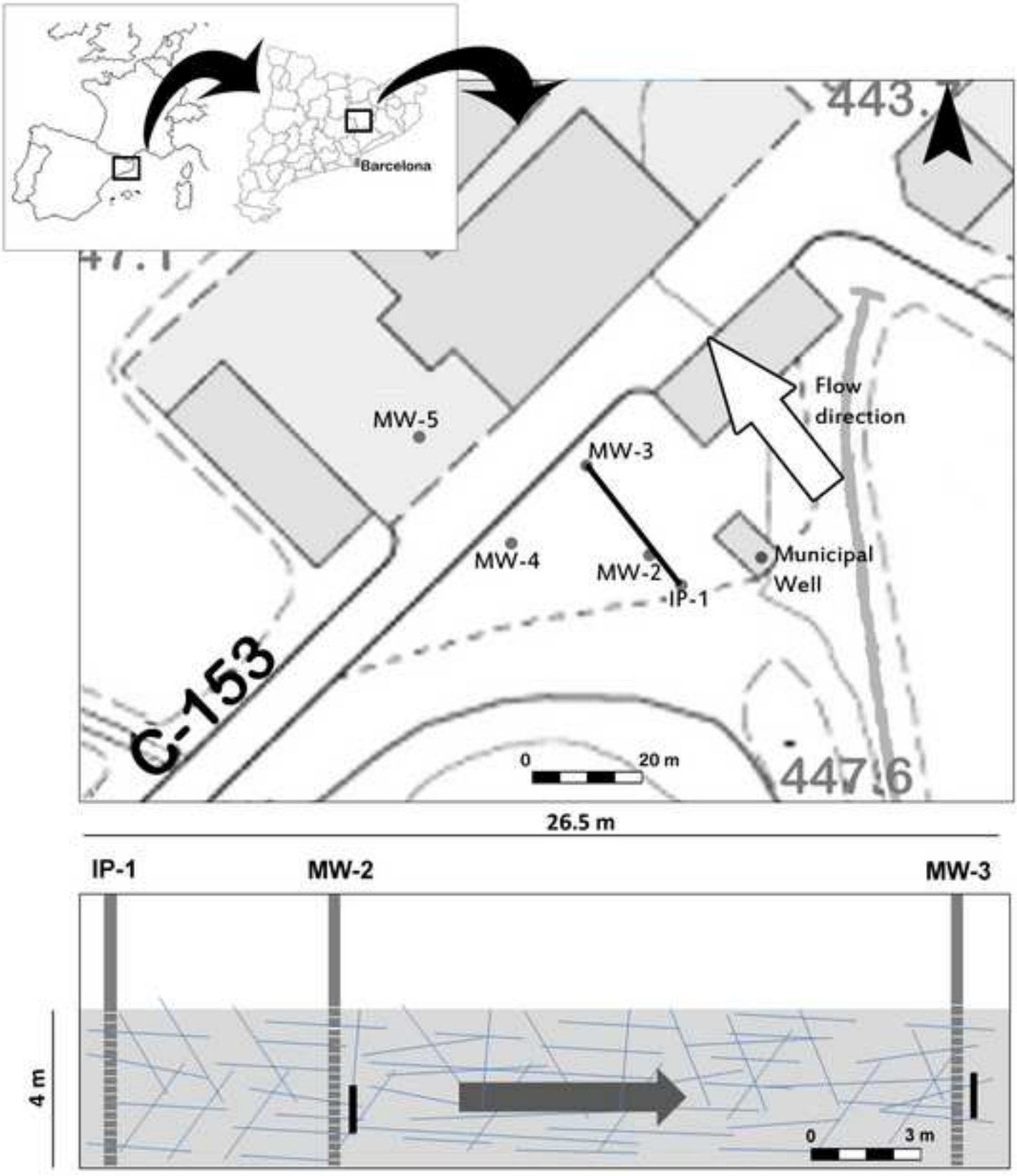

Figure 2

Click here to download high resolution image

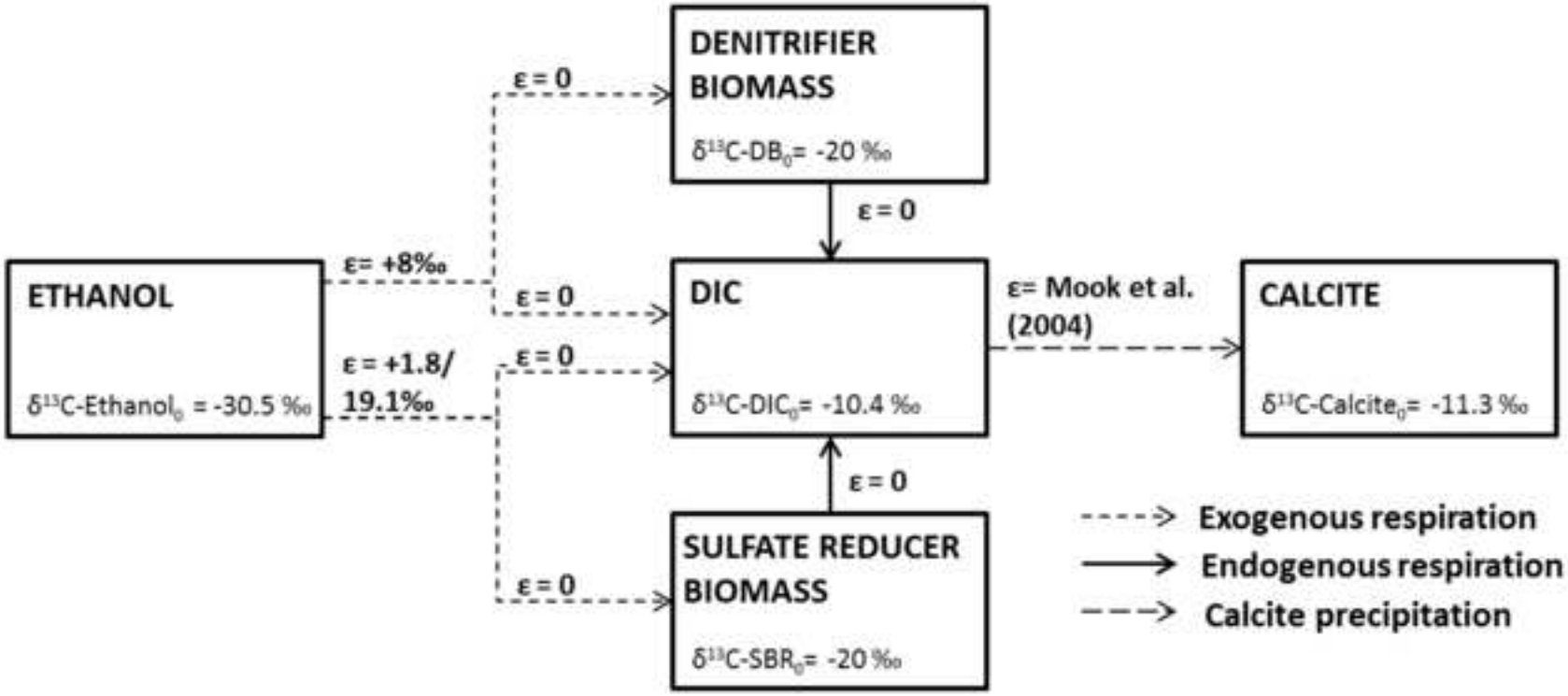

Figure 3

Click here to download high resolution image

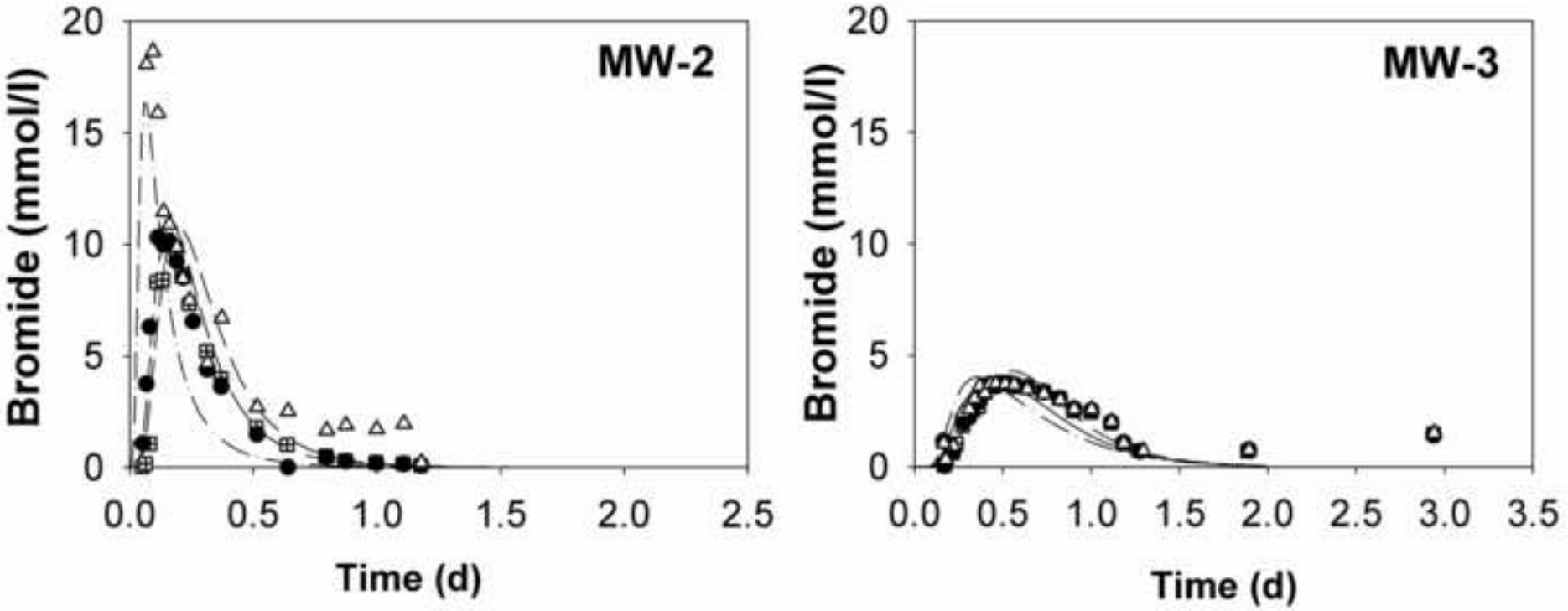

Figure 4

Click here to download high resolution image

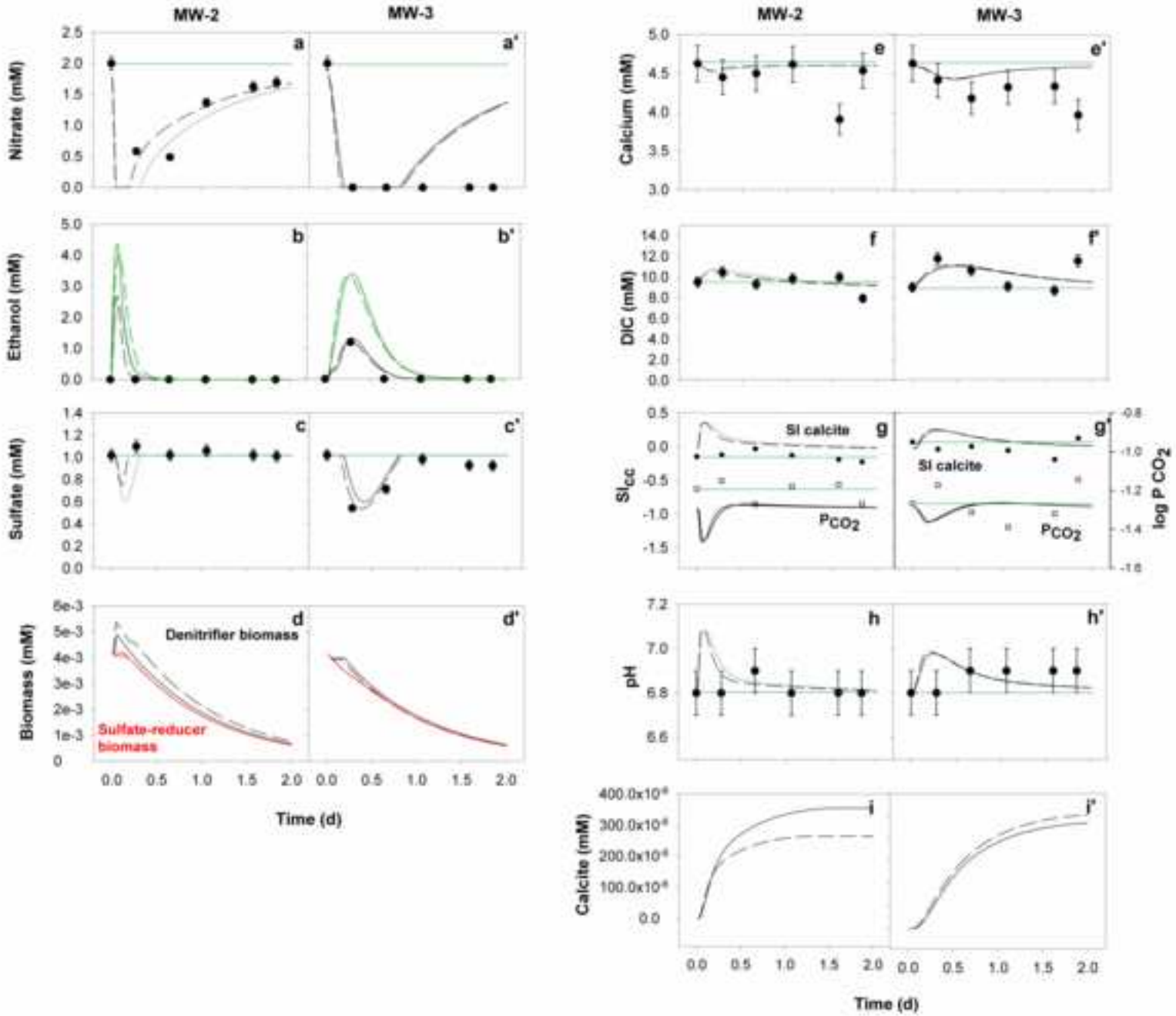

Figure 5

Click here to download high resolution image

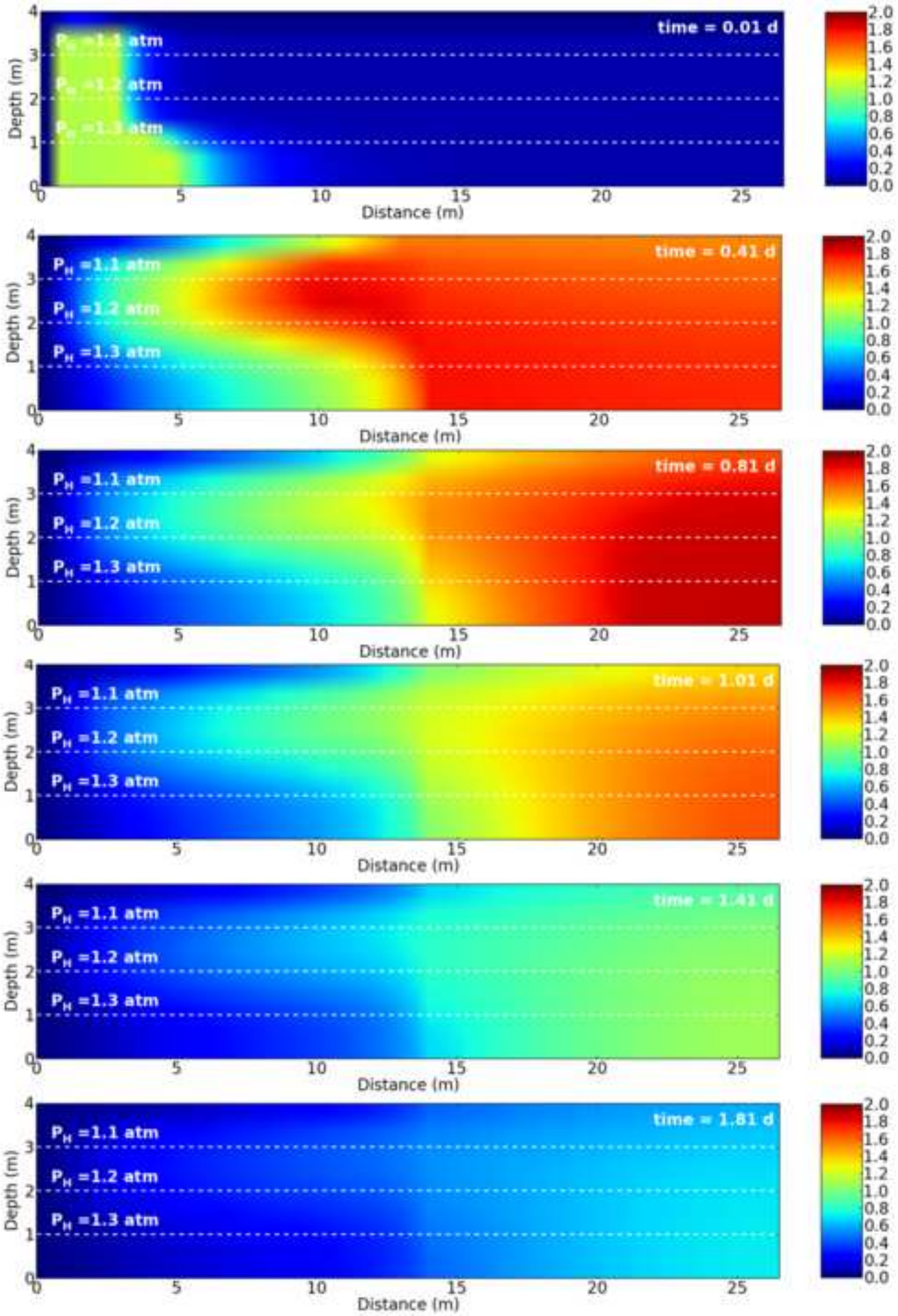

Figure 6

Click here to download high resolution image

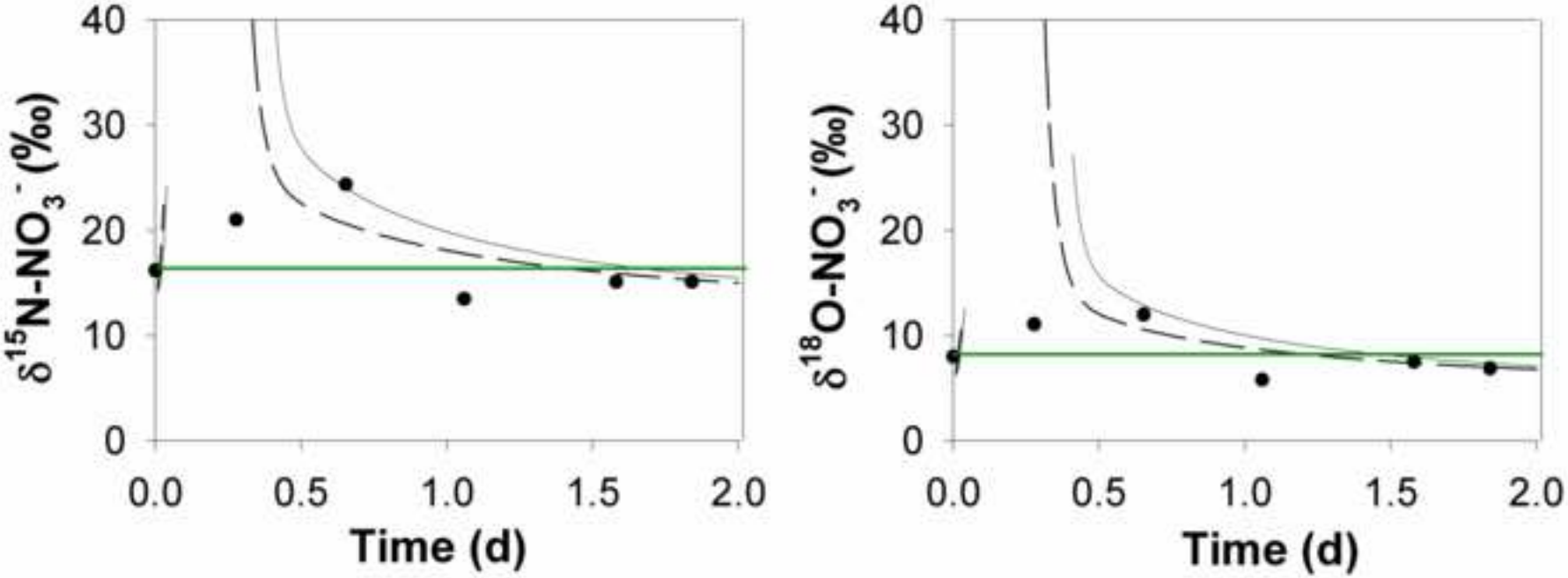

Figure 7

Click here to download high resolution image

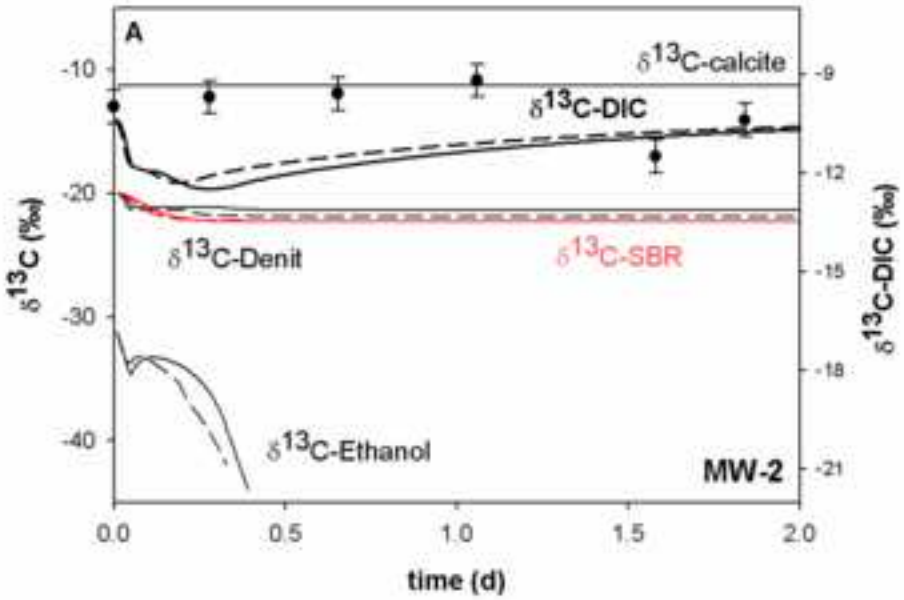

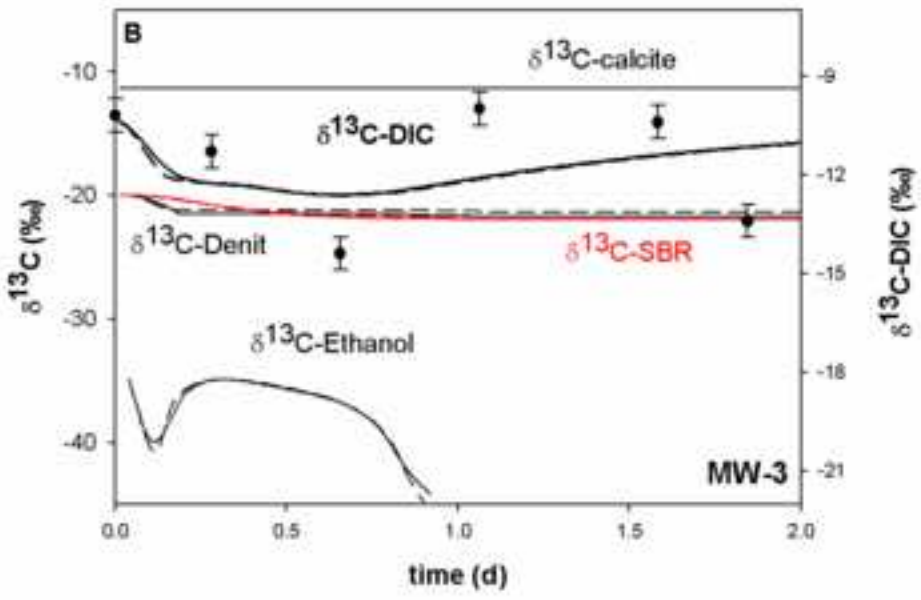

Figure 8

Click here to download high resolution image

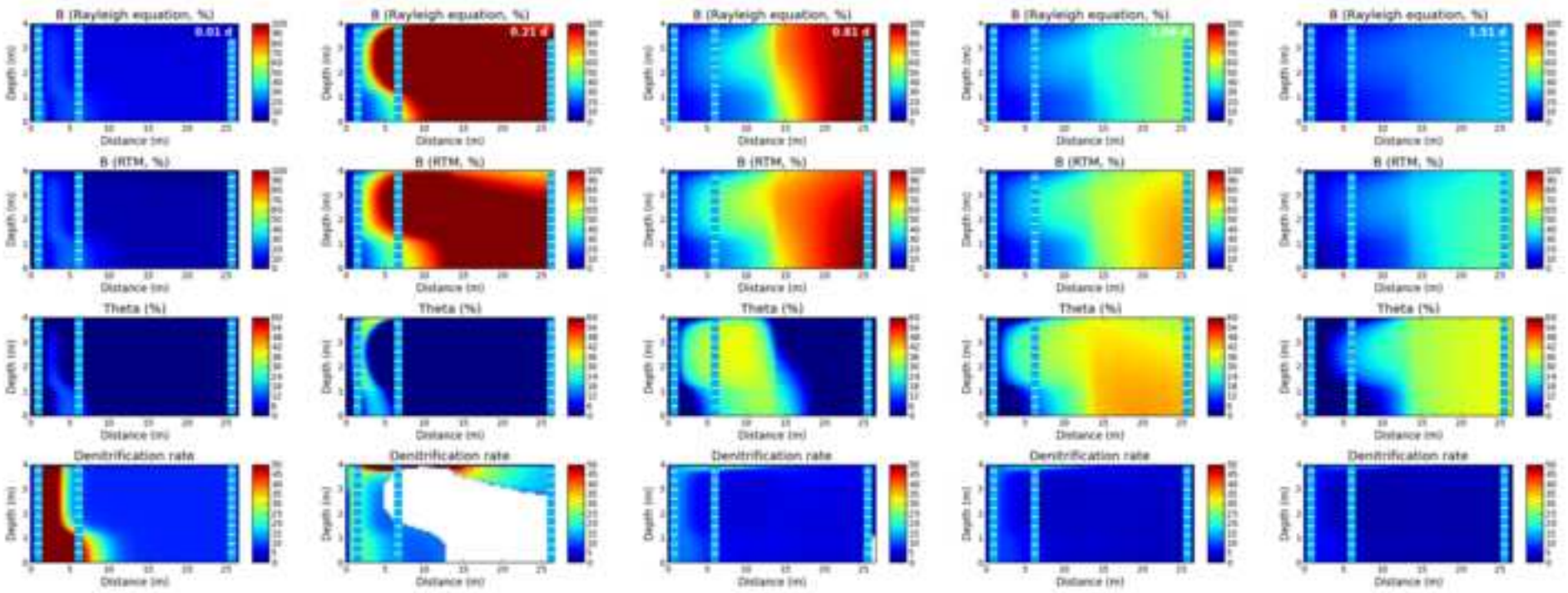

Table 1

Click here to download Table: 2-Rodriguez-Escales_TABLE 1_v2_r1.docx

Table 1. Reactive processes involved in biogeochemical modeling.

Reactive processes		**Equation**	
Biological processes (for nitrate and sulfate reduction)	Exogenous respiration rate	$r_{ED} = -k_{max}\frac{[ED]}{[ED]+K_{S,ED}}\frac{[EA]}{[EA]+K_{S,EA}}[X]$	(5)
		$r_{EA} = Qr_{ED} - Sb[X]$	(6)
	Biomass rate	$r_X = -Y_h r_{ED} - b[X]$	(7)
Geochemical interaction	Calcite precipitation	$r_{min,prep} = K_{obs}(\Omega - 1)$	(8)
		$\Omega = \frac{IAP}{K}$	(9)
Stable isotope geochemistry model (general rates)	Light isotopes	$r_{Z,l} = r_Z\frac{[Z_l]}{[Z_l]+[Z_h]}$	(10)
	Heavy isotopes	$r_{Z,h} = r_Z\frac{[Z_h]}{[Z_l]+[Z_h]}(\varepsilon + 1)$	(11)

ED [ML^{-3}] electron donor concentration
EA [ML^{-3}] electron acceptor concentration
X [ML^{-3}] biomass concentration
k_{max}[T^{-1}] is the maximum consumption rate of the electron donor (calibrated parameter)
$K_{s\,ED}$ [$M\,L^{-3}$] and $K_{s\,EA}$ [$M\,L^{-3}$] are the half-saturation constants (calibrated parameter)
Q [-] and Y_h[-] are stoichiometric parameters (determined in Reactions 1 and 2)
S [-] is stoichiometric parameter for endogenous respiration (0.92, internally calculated by Phreeqc)

b [T^{-1}] is the decay constant (calibrated parameter)
K_{obs} [$ML^{-3}T^{-1}$] is the precipitation rate constant
Ω [-] is the saturation state of calcite (calculated)
IAP is the ion activity product
K is the thermodynamic equilibrium constant at 15°C (from Phreeqc database)
ε (‰) is the isotopic enrichment factor (from Vidal-Gavilan et al. 2013; Rodríguez-Escales et al. 2014 and Goevert and Conrad (2008)).

Table 2

Click here to download Table: 2-Rodriguez-Escales_TABLE 2_v2_r1.docx

Table 2. Equations and enrichment factors considered in carbon isotope network

Process	^{13}C Rate	Kinetic isotope enrichment factor (ε)
Oxidation of electron donor: Ethanol→ DIC	$r_{^{13}C\text{-}BM} = Y_h r_{ED} \frac{[ED_h]}{[ED_l]+[ED_h]}(\varepsilon_{ED/BM}+1)$	Denitrification +8 ‰ (Rodríguez-Escales et al., 2014) Sulfate Reduction +1.8/-19.1‰ (Goevert and Conrad, 2008)
Biomass Growth: Ethanol→ Biomass	$r_{^{13}C\text{-}DIC} = Pr_{ED} \frac{[ED_h]}{[ED_l]+[ED_h]}(\varepsilon_{ED/DIC}+1)$	Denitrification +8 ‰ (Rodríguez-Escales et al., 2014) Sulfate Reduction +1.8/-19.1 ‰ (Goevert and Conrad, 2008)
Biomass Decay: Biomass→ DIC	$r_{^{13}C\text{-}DIC} = R[X]b$	0 (Rodríguez-Escales et al., 2014)
Calcite Precipitation: DIC→ Calcite	as Mook et al. (2004)	calculated from van Breukelen et al. (2004) and Mook et al. (2000) considering a temperature of 15ºC: $\varepsilon_{a/b}$ =10.12 ‰; $\varepsilon_{c/b}$ =-0.49 ‰; $\varepsilon_{c/b}$ =+0.41 ‰ (where a is CO_2, b HCO_3^-, c $CO_3$2- and s $CaCO_3$)

Table 3

Click here to download Table: 2-Rodriguez-Escales_TABLE 3_v2_r1.docx

Table 3. Concentrations of the aquifer and the injection solution used for the model. Data from Vidal-Gavilan et al. (2013).

Parameter	Unit	Aquifer solution	Injected solution
		Value	Value
Ethanol	mM		13.7
Nitrate	mM	2.0	2.0
DIC	mM	9.5	9.5
pH		6.7	6.7
Temperature	ºC	15	15
Chloride	mM	1.4	1.4
Sulfate	mM	1.0	1.0
Calcium	mM	4.6	4.6
Sodium	mM	2.2	2.2
Magnesium	mM	1.4	1.4
Potassium	mM	2.4	2.4
$\delta^{15}N\text{-}NO_3^-$	‰	16.2	16.2
$\delta^{18}O\text{-}NO_3^-$	‰	8	8
$\delta^{13}C$-DIC	‰	-11.8	-11.8
$\delta^{13}C$-Ethanol	‰		-30.5

Table 4

Click here to download Table: 2-Rodriguez-Escales_TABLE 4_v2_r1.docx

Table 4. Comparison of parameters between the batch scale and the field scale. (1) Rodríguez-Escales et al. (2014) (2) Nagpal et al. (2000).

	DENITRIFICATION		**SULFATE-REDUCTION**	
	Batch scale[1]	Field scale	Batch scale[2]	Field scale
Y_h (mol C-biomass/mol C-ethanol)	0.7	0.7		1.0
Q (mol C-ethanol/ mol nitrate-sulfate)	1.9	1.9		7.5
K_{max} (mol C-ethanol/mol C-biomass d)	$1.1x10^{2}$	$1.1x10^{2}$	$5.2x10^{1}$	$5.2x10^{1}$
K_{sat} C-ethanol (M)	$1.5x10^{-1}$	$1.3x10^{-1}$	$9.0x10^{-3}$	$1.3x10^{-1}$
K_{sat} nitrate (M)	$1.7x10^{-4}$	$1.4x10^{-5}$		
K_{sat} sulfate (M)			$8.5x10^{-3}$	$5x10^{-3}$
b (d^{-1})	0.15	0.95	-	0.95
K prep (M d^{-1})	8.6×10^{-6}	4.3×10^{-4}		

Table 5

Click here to download Table: 2-Rodriguez-Escales_TABLE 5_v2_r1.docx

Table 5. Parameters from denitrification models at different scales and using different electron donors.

Source	Scale	Processes considered	Electron donor used	Parameters				
				Y_h	Q	b	$K_{sat\ oc}$	$K_{sat,\ nit}$
				(mol C-cel mol C-OC^{-1})	(mol C-OC-mol nitrate^{-1})	d^{-1}	(mol C-OC L^{-1})	(mol nitrate L^{-1})
Rodríguez-Escales et al. (2014)	Batch scale	Nitrate respiration Microbial growth and decay	Ethanol	0.73	1.89	0.15	1×10^{-1}	1.7×10^{-4}
Mastrocicco et al. (2011)	Batch scale	Nitrate respiration Microbial growth and decay	Acetate	0.35	1.25	-	1×10^{-3}	1×10^{-4}
Lee et al. (2006)	Field (Sedimentary aquifer)	Nitrate respiration Microbial growth and decay	Natural organic matter	-	-	0.06	1.7×10^{-4}	1.2×10^{-5}
Chen and MacQuarrie (2004)	Field (Sedimentary aquifer)	Nitrate respiration Geochemical interaction Isotope geochemistry	Natural organic matter	0.05	-	0	8.3×10^{-6}	1.6×10^{-6}
Killingstad et al. (2002)	Batch scale	Nitrate respiration	Natural organic matter	0.19	-	0.01	2.2×10^{-5}	1.4×10^{-5}
	Field (Sedimentary aquifer)	Nitrate respiration	Natural organic matter	0.19	-	0.01	2.2×10^{-5}	1.4×10^{-5}
Kornaros and Lyberatos (1998)	Batch scale	Aerobic respiration Nitrate respiration Microbial growth and decay	Glutamate	0.61	1.05	-	2.5×10^{-4}	5.5×10^{-5}
Clement et al. (1997)	Batch scale	Nitrate respiration Microbial growth and decay	Acetate	0.20	0.96	0.06	4.1×10^{-5}	1.1×10^{-5}
Kinzelbach et al. (1991)	Field (Sedimentary aquifer)	Nitrate respiration Microbial growth and decay	Hydrocarbon (aliphatic and aromatic)	0.2	-	0.2	6.6×10^{-4}	3.2×10^{-6}
			RANGE	**(0.05-0.73)**	**(0.96-1.89)**	**(0-0.2)**	**(8.3×10^{-6}-1 x 10^{-1})**	**(1×10^{-6} - 1.7×10^{-4})**

Background dataset for online publication only

Click here to download Background dataset for online publication only: 2-Rodriguez-Escales_SUPPORTING INFORMATION_r1.d